Dynamic organization of ligand-grafted nanoparticles during adsorption and surface compression at fluid-fluid interfaces

Axel Huerre,[†,‡] Fernando Cacho-Nerin,[¶,‡] Vincent Poulichet,[†,§] Christiana E. Udoh,[†] Marco De Corato,[†] and Valeria Garbin*,[†]

†*Department of Chemical Engineering, Imperial College London, London SW7 2AZ, United Kingdom*

‡*A. H. and F. C.-N. contributed equally*

¶*Diamond Light Source, Harwell Science and Innovation Campus, Didcot OX11 0DE, United Kingdom*

§*Current address: Complex Fluids Group, School of Chemical Engineering, UNSW Sydney, Sydney, Australia*

E-mail: v.garbin@imperial.ac.uk

Abstract

Monolayers of ligand-grafted nanoparticles at fluid interfaces exhibit a complex response to deformation due to an interplay of particle rearrangements within the monolayer, and molecular rearrangements of the ligand brush on the surface of the particles. We use grazing-incidence small-angle X-ray scattering (GISAXS) combined with pendant drop tensiometry to probe *in situ* the dynamic organization of ligand-grafted nanoparticles upon adsorption at a fluid-fluid interface, and during monolayer compression. Through the simultaneous measurements of interparticle distance, obtained from

1

GISAXS, and of surface pressure, obtained from pendant drop tensiometry, we link the interfacial stress to the monolayer microstructure. The results indicate that, during adsorption, the nanoparticles form rafts that grow while the interparticle distance remains constant. For small-amplitude, slow compression of the monolayer, the evolution of the interparticle distance bears a signature of ligand rearrangements leading to a local decrease in thickness of the ligand brush. For large-amplitude compression, the surface pressure is found to be strongly dependent on the rate of compression. Two-dimensional Brownian Dynamics simulations show that the rate-dependent features are not due to jamming of the monolayer, and suggest that they may be due to out-of-plane reorganization of the particles (for instance expulsion or buckling). The corresponding GISAXS patterns are also consistent with out-of-plane reorganization of the nanoparticles.

Introduction

Nanoparticle monolayers at fluid-fluid interfaces find a wide range of applications, from advanced materials,[1–3] to catalysis,[4] sensors,[5] and controlled release.[6] Nanoparticles can either form monolayers at fluid interfaces by spontaneous adsorption from a suspension[4,7–9] (Gibbs monolayers), or they can be cast at an interface from a volatile spreading solvent[10–13] (Langmuir monolayers). The organization of the nanoparticles within the monolayer, which affects the properties and function of the resulting film,[5,8,10] depends on the interparticle interactions, and how they are modified when the particles are confined at the interface.[14] The interactions between nanoparticles grafted with capping ligands or polymers can be dominated by the grafted layer, particularly when its thickness is comparable to the size of the nanoparticle core. Molecular simulations predict ligand rearrangements upon nanoparticle adsorption at the interface between two fluid phases[15,16] due to the asymmetric environment (dielectric constant and solvent quality) surrounding the particle. Because of the deformability of the grafted layer, these core-shell systems effectively behave as soft nanoparticles. The resulting interparticle interactions have been characterized in simulations[17] and measured

experimentally.[18]

The dynamics of nanoparticle monolayers upon interface deformation affect complex multiphase flows of relevance to industrial processes, for instance emulsification. When a monolayer of nanoparticles deforms under flow, the dilation or compression of the interface causes an evolution of the microstructure, which in turn determines the mechanical response of the interface and the overall behavior of the multiphase system.[19] The structural evolution of nanoparticle monolayers upon compression has been the subject of numerous studies.[11–13,18,20] It is now well understood that, for strong area compression, the monolayer deforms out of the plane of the interface, leading to buckling of the monolayer,[12,13] or particle expulsion.[9] A commonly used method to determine the microstructure of Langmuir monolayers is the Langmuir-Blodgett technique, where a sample is lifted off the interfacial film onto a solid substrate, and imaged *ex situ* by transmission electron microscopy.[10,13] The surface pressure generated by the particle monolayer can be monitored using a Wilhelmy plate.[11–13,18,20] A possible limitation of this method is that the evaporation of the subphase upon drying of the sample prior to imaging may alter the microstructure. *In situ* methods to characterize nanoparticle monolayers at fluid interfaces include X-ray reflectivity or small-angle X-ray scattering, which have been used both on Langmuir and Gibbs monolayers. These techniques give access to the real-time evolution of the microstructure, for instance during compression in a Langmuir trough,[11,20] or in evaporating droplets.[21–23] Grazing-incidence small-angle X-ray scattering (GISAXS) is well-suited to study interfaces and layered materials, since in this geometry the technique is highly sensitive to the in-plane order of a material, as well as to changes in its thickness. *In situ* atomic force microscopy of a nanoparticle monolayer at a liquid interface has been used to compare real-space imaging with GISAXS, and to corroborate the correspondence between microstructure determination in real and reciprocal space.[24]

Here we use for the first time GISAXS combined with pendant drop tensiometry to study *in situ* the dynamic organization of ligand-grafted nanoparticles at a fluid-fluid interface.

The two simultaneous measurements enable us to link the interfacial stress to the monolayer structure, and to reveal the underlying mechanisms of non-equilibrium phenomena. We study a model system of ligand-grafted nanoparticles, namely 4.5-nm gold cores grafted with a thiolated $C_{11}E_4$ surfactant, at the interface between water and a fluorinated oil. The interparticle interactions depend on the configuration of both the hydrophobic block (undecane, contour length ~ 1.7 nm) and the hydrophilic block (tetraethylene glycol, contour length ~ 1.9 nm). Molecular dynamics simulations have shown that the configuration of the two blocks depends both on the solvent conditions, and on the grafting density of the ligands.[15] This system has been previously characterized and is known to exhibit spontaneous adsorption from suspension,[7] a soft repulsive interparticle potential[18] leading to colloidal stability at the interface, and particle expulsion upon area compression.[9] Interestingly, the dynamic behavior of the nanoparticle monolayer upon compression depends on the rate of deformation.[18] The question remains open of whether rate-dependent behaviors of ligand-grafted nanoparticles are due primarily to nanoparticle rearrangements within the monolayer, or to ligand rearrangements on the nanoparticles. To address this question, we characterise the microstructural organisation of the nanoparticle monolayer during adsorption at the fluid interface, and upon compression at different rates. We compare the experimental results on compression with the results of Brownian Dynamics simulations to assess the effects of nanoparticle rearrangements within the monolayer.

Experimental Section

Materials and sample preparation. Spherical gold (Au) nanoparticles with a hard-core radius $a_{core} \approx 2.3$ nm, functionalized with capping ligand mercaptoundecyl tetra(ethylene glycol) (MUTEG), were obtained from Sigma-Aldrich. The capping ligand is uncharged and provides stability to the colloidal suspension by short-range steric repulsion. The grafting density of the ligands on the particles is not known a priori. The aqueous nanoparticle
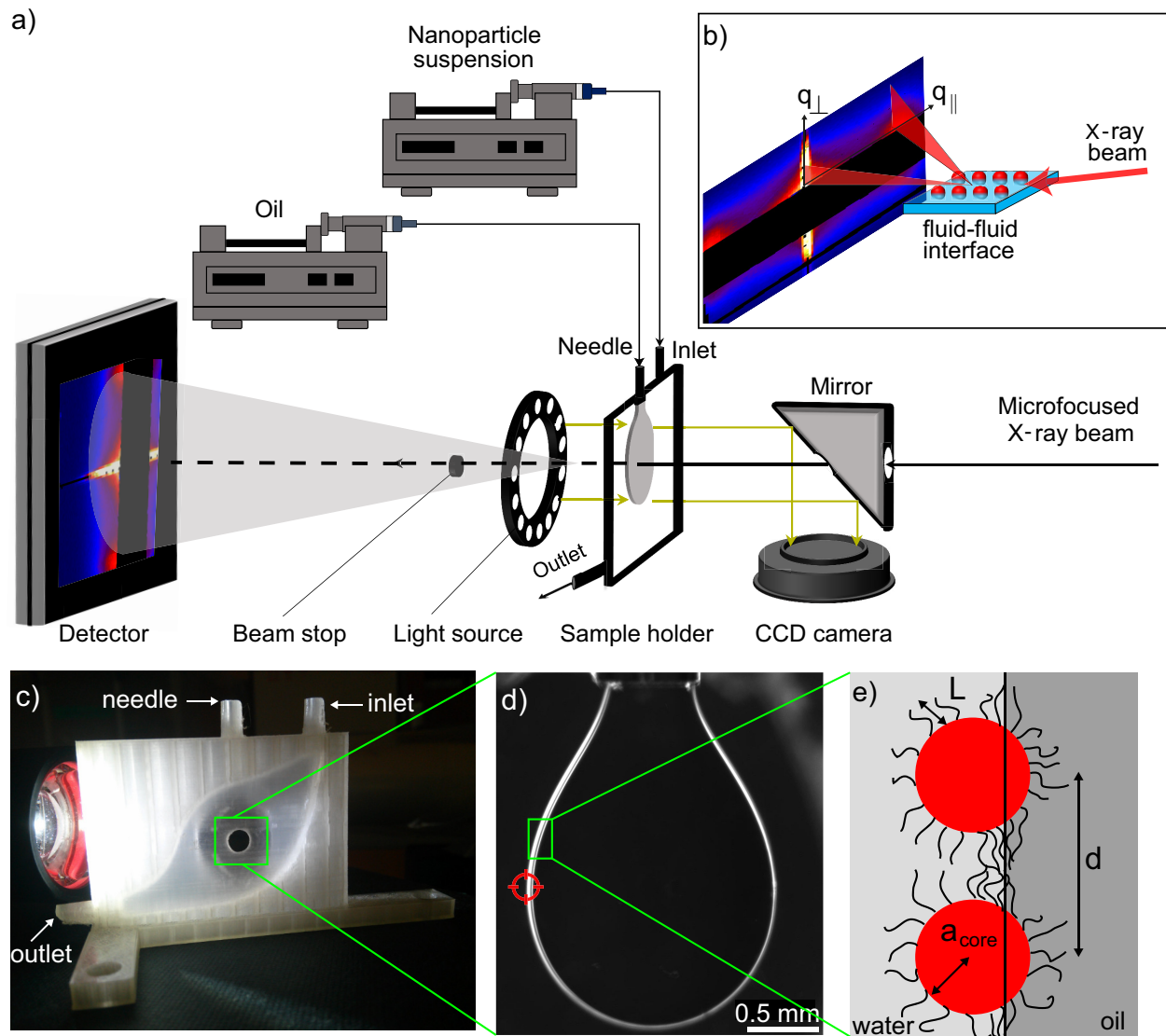
Figure 1: Experimental setup and notations. (a) Schematic of the pendant-drop setup adapted to the constraints of a GISAXS experiment. (b) Schematic of the GISAXS measurement principle. The data are recorded on the detector in the $(q_\parallel, q_\perp)$ plane. (c) Custom-made, 3D-printed sample cell. (d) An optical image of the pendant drop. The red viewfinder indicates the point where the X-ray beam hits the interface. (e) Notation used in the text to describe the adsorbed particles of radius a_{core} covered with MUTEG ligands stretched at a length L, and with center-to-center distance d.

suspension was diluted in ultrapure water to give a bulk concentration $n \approx 2.5 \times 10^{14}$ NPs/mL (corresponding to a volume fraction $\approx 10^{-5}$). Fluorinated oil octafluoropentyl acrylate (OFPA) was obtained from Sigma-Aldrich and used as received. Syringes, tubing and needles in contact with the fluid phases (see below) were cleaned from surface active impurities prior to the experiments using ethanol, and rinsed with ultrapure water.

Experimental setup. The experiment was carried out at beamline I22 of Diamond Light Source (UK). The experimental setup, shown schematically in Figure 1a, was designed to perform GISAXS (see schematic in Figure 1b) on the curved surface of a pendant drop. A custom-made fluidic cell (Figure 1c) holds a needle vertically in place, and has an inlet and an outlet to exchange the outer fluid. The outer phase (nanoparticle suspension) and the drop phase (oil) are injected using syringe pumps (Harvard Apparatus). The pump that regulates the drop volume is controlled remotely to impart compression by incremental withdrawals of oil. The entry and exit windows of the cell are made of scratch-free mica to minimize background scatter. The window on the downstream side of the cell is sufficiently large to collect both the small- and wide-angle scattering signal. The distance between the windows (5 mm) was optimized for a photon energy of 14 keV, which is optimal for gold as it is just below the L_1 absorption edge. At this wavelength, the attenuation length of water is just over 5 mm, and provides a balanced middle point between absorption and scattering signal in solution. This distance allowed a maximum droplet diameter of 3 mm, with a 1 mm external water layer to avoid boundary effects. The cell is mounted on an xyz micropositioning stage (Physik Instrumente, Germany), so the droplet can be positioned and scanned with respect to the X-ray beam. The experiment was carried out using a microfocus setup, which focuses the beam to a spot of 10 μm (FWHM) as illustrated by the red viewfinder in Figure 1d. At 14 keV, the depth of focus is sufficiently long to cover the footprint of the beam on the droplet surface. The setup also features an in-line optical microscope consisting of a long-working-distance objective with 50-500$\times$ magnification (model VH-Z50L, Keyence, UK) connected

to a digital camera, which provides a live optical image of the sample. The objective and camera are positioned on a horizontal axis perpendicular to the beam, and view the sample through a 45° mirror with a 1 mm diameter hole to let the X-ray beam through. The exact position of the beam in the camera frame was calibrated prior to the experiment. To image the drop in transmission, a light ring (LED RingLight Ultrabright, GX Microscope) was positioned downstream of the X-ray beam. The lighting conditions resulted in a "negative" image of the drop, shown in Figure 1d. X-ray scattering data was collected on a Pilatus 3 2M detector (Dectris, Switzerland) positioned 1 m away from the sample. In order to minimize air scattering, this space was filled with helium. In addition, downstream of the cell a 200 μm diameter tungsten wire was positioned in close proximity, to act as the primary beam stop. A small lead disc was affixed to the face of the detector as an additional beam stop. For each acquired frame on the detector, a corresponding optical image of the droplet was recorded, so that the surface tension could be extracted by image analysis. Because the position of the equator changes with the droplet volume, the cell was repositioned after each incremental withdrawal. Similarly, the cell had to be repositioned during adsorption experiments, because the shape of the drop changed with decreasing surface tension upon nanoparticle adsorption, and the position of the interface moved with respect to the X-ray beam. For each state, three frames were acquired by scanning across the liquid-liquid interface, with a step size of 10 μm, corresponding to the beam size.

Surface tension measurements. The optical images of the drop were used for drop-shape analysis to extract the effective surface tension, γ, of the particle-laden interface. The surface pressure generated by the nanoparticle monolayer, Π, was calculated as $\Pi = \gamma_0 - \gamma$, where $\gamma_0 = 26$ mN m^{-1} is the surface tension of the bare OFPA-water interface. The images where analysed in ImageJ. An edge detection routine and a threshold were applied to obtain the contour of the drop. A Young-Laplace fitting algorithm, available as open-source ImageJ plugin Pendent_Drop,[25] was then used to fit the surface tension, the drop volume, and the

drop surface area. The uncertainty introduced by the edge detection routine leads to a typical error of ± 0.1 mN/m on the determined value of the surface tension and less than 0.1 % for the area.

GISAXS data analysis. A transmission experiment was carried out with an X-ray sensitive diode, to test the reliability of the data captured by the detector, by measuring the oil and water refractive indices in our experimental configuration (see Supporting Information, Figure S1). Before fitting the data, a pre-processing step consisting in re-orienting the obtained signal was performed for each data-set (Supporting Information, Figure S2). A line cut at fixed $q_\perp = 0.034$ Å^{-1} was extracted by integrating the whole frame between 0.0327 and 0.0371 Å^{-1}, which represents a 5 pixel thick region. This provided a good balance between robustness in the profile extraction and signal smear due to the integration over the $q_\perp$ axis. The extracted $q_\parallel$ profiles were then analyzed using Igor Pro (Wavemetrics, OR, USA). Each profile was normalized to the exposure time prior to fitting to a Lorentzian peak on a linear baseline. This provided a good approximation to the scattering profile in the vicinity of the correlation peak.

Brownian Dynamics simulations. We performed two-dimensional Brownian dynamics simulations of the nanoparticle monolayer, assuming that the nanoparticles are irreversibly adsorbed on the interface. At the interface, the ligands are stretched over a length L, and when the particles are in contact, the center to center distance d is simply $d = 2a_{\text{core}} + 2L$ (see Figure 1e). We consider N_d disks of radius a_{core} in a circular domain of radius R_{box}. The domain radius is fixed as $R_{\text{box}} = 100 \, a_{\text{core}}$. The steric repulsion force between two particles i and j caused by the overlap of the ligand brushes is modelled through the Alexandre-De Gennes potential, recently used to model similar systems:[11,18]

$$U_{ij}\left(d_{ij}\right) = -\pi\, k_B T\, a_{\text{core}}\, \sigma^{3/2} \left[\frac{-16\left(2\,L\right)^{2.25}}{5\left(d_{ij} - 2a_{\text{core}}\right)^{0.25}} + \right.$$

$$\left. + \frac{16\left(d_{ij} - 2a_{\text{core}}\right)^{2.75}}{77\left(2L\right)^{0.75}} - \frac{96\,L}{35}\left(d_{ij} - 2a_{\text{core}}\right) + \frac{192\,L^2}{11} \right]. \quad (1)$$

In Eq. (1), k_B is the Boltzmann constant, T is the absolute temperature, σ is the grafting density of the ligands, L is the thickness of the ligand brush and d_{ij} is the center-to-center distance between particles i and j. A plot of the interaction potential is given in Supporting Information (Figure S4).

The evolution of the particle position vector $\boldsymbol{r_i}$ is computed, and the displacement vector $\Delta \boldsymbol{r_i}$ over each time step is obtained by modifying a standard Brownian dynamics algorithm[26] to include the effect of the monolayer compression:

$$\Delta \boldsymbol{r_i} = \sqrt{2\, D\Delta t}\, \boldsymbol{\zeta}_i - \sum_{j \neq i} \frac{D\,\Delta t}{k_B T} \frac{\partial U_{ij}}{\partial d_{ij}}\, \hat{\boldsymbol{d}}_{\boldsymbol{ij}} + \frac{1}{2}\dot{\alpha}(t)\Delta t\, \boldsymbol{r_i}. \quad (2)$$

The first term on the right hand side represent the classic nanoparticle diffusion with a diffusion coefficient D. The second term represents the displacement due to the interparticle repulsive force $\frac{\partial U_{ij}}{\partial d_{ij}}\, \hat{\boldsymbol{d}}_{\boldsymbol{ij}}$, with $\hat{\boldsymbol{d}}_{\boldsymbol{ij}}$ a unit vector directed from particle i to particle j. The effects of the flow field induced by the compression of the monolayer at a rate $\dot{\alpha}(t) = -\frac{1}{A(t)}\frac{dA(t)}{dt}$ are taken into account in the last term of Eq. (2). A cutoff distance of $2a_{\text{core}} + 2L$ is used for the steric repulsive force.

A monolayer of nanoparticles is initialized with random positions and the system is allowed to equilibrate for a time $40\, a_{\text{core}}^2/D$ by solving Eq. (2) with $\dot{\alpha}(t) = 0$. After the equilibration, compression starts with a constant $\frac{dA(t)}{dt}$ by changing $R_{\text{box}}(t) = 100\, a_{\text{core}}\sqrt{1 + \dot{\alpha}(0)\, t}$. The surface pressure Π of the monolayer is given by:

$$\Pi = \frac{\left(N_d k_B T + \frac{1}{2}\sum_{i=1}^{N_d}\sum_{j \neq i}\frac{\partial U_{ij}}{\partial d_{ij}} d_{ij}\right)}{\left(\pi\, R_{\text{box}}^2(t)\right)}. \quad (3)$$

Results and Discussion

Measurement of interparticle distance during adsorption.   We studied the particle adsorption process by simultaneously monitoring the structure of the film by GISAXS, and the dynamic surface tension by drop shape analysis. The oil drop is created using a needle inserted in the nanoparticle suspension, and the evolution of both the surface tension and the interparticle distance is probed. Figure 2 illustrates the data analysis process. Starting from the GISAXS-remapped state (Figure 2a), a line cut at fixed $q_\perp = 0.034$ Å^{-1} is extracted. Figure 2b shows the resulting SAXS profiles and the corresponding fits around the correlation peak for the adsorption process. The confidence of the fits was typically around 1% of the fitted value, as measured by the estimated standard deviation of the fitted parameter. A plot of $q_\parallel$ with error bars is given in Supporting Information (Figure S3). Data were acquired every 5 minutes (300 seconds) for 80 minutes (4800 seconds). As adsorption proceeds, the density of particles at the interface increases, the peaks in the X-ray scattering signal become narrower and their spacing progressively decreases. The profiles have been offset vertically for clarity, but at high $q_\parallel$ values they all coincide, indicating a consistent background level. The first profile in the time series is significantly different from the others, clearly indicating that the film is only just beginning to form and there is still no order in it. Thus, although the chosen peak shape fits the data well, the resulting average interparticle distance must be considered with caution for this first point. The correlation peak (found for $q_\parallel = q_m$) is interpreted as the first reflection of a hexagonal lattice. Hexagonal arrangement is usually found for nanoparticles at interfaces[27–31] and q_m thus represents the average inter-particle distance in the film. Figure 2c shows the time evolution of the interparticle distance, after conversion into real space using the formula $d = \frac{4\pi}{\sqrt{3}} \frac{1}{q_m}$. The uncertainty in acquisition time ($\pm$ 60 s) is represented by the width of the filled circles, and the uncertainty from the fit of the peak position is better than the symbol height. A discussion on error determination in our experimental configuration is provided in Supporting Information. The first data point is obtained after 1200 s of incubation as the resolution of the correlation peak at earlier times

does not give a reliable distance measurement. Remarkably, it is observed that the distance decreases rapidly to a approximately constant value $d \approx 10$ nm.
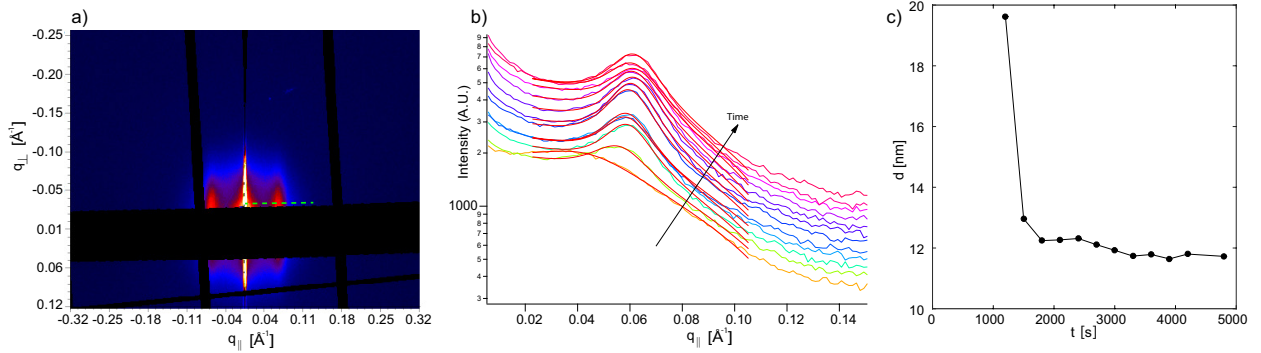

Figure 2: Temporal evolution of SAXS signal during nanoparticle adsorption. (a) Image acquired on the X-ray sensor. (b) Intensity of the GISAXS signal as a function of the wave vector $q_\parallel$ at different times during adsorption. The fits allow to extract the position of the local maximum q_m. (c) Interparticle distance d as a function of time, obtained as $d = \frac{4\pi}{\sqrt{3}} \frac{1}{q_m}$.

Evolution of interparticle distance and surface tension during adsorption. Optical images of the droplet acquired during the adsorption process at the same times as the GISAXS measurements were used to extract the evolution of the interfacial tension γ. The results are reported in Figure 3a together with the interparticle distance d. The surface tension decreases from an initial value $\gamma_0 = 26$ mN m^{-1} for the bare water-OFPA interface to a constant value of $\gamma_\infty = 16$ mN m^{-1} after an adsoprtion time of approximately 4000 s. The magnitude of the decrease in surface tension is consistent with previous studies using the same system.[7,9] The inset in Figure 3a shows the time derivatives of the distance, $\Delta d / \Delta t$, and of the surface tension, $\Delta \gamma / \Delta t$, as a function of time. It can be seen that the two derivatives plateau to 0 at different times, $\tau_1 \approx 2000$ s and $\tau_2 \approx 4200$ s, respectively.

Figure 3b illustrates the possible scenarios of the nanoparticles adsorption dynamics occurring before and after τ_1. At early times, the adsorption process consists of a constant evolution of a hexagonal network of nanoparticles at the interface. Each time a nanoparticle is adsorbed, the whole network reorganizes, reducing the interparticle distance and preserving the hexagonal arrangement. This scenario would result in a decrease of surface tension
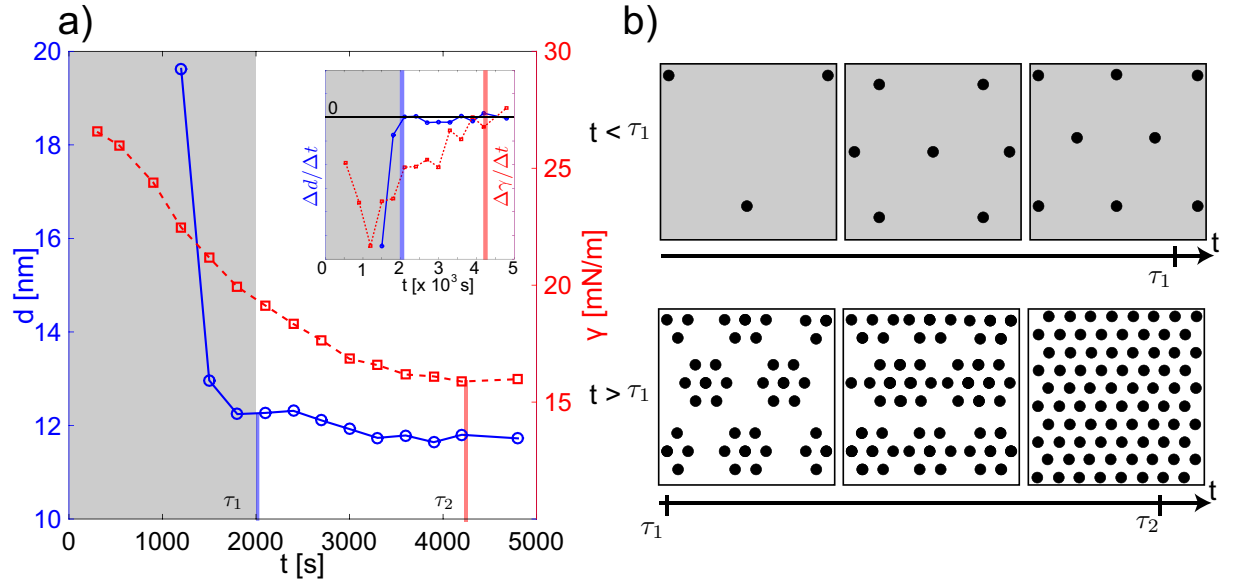
11

Figure 3: Nanoparticle adsorption experiment. (a) Interparticle distance d (circles) and surface tension γ (squares) as a function of time during adsorption. Inset: derivatives of d and γ as a function of time. The vertical lines mark $\tau_1 \approx 2000$ s and $\tau_2 \approx 4200$ s, the time scales for which d and γ, respectively, become approximately constant. (b) Schematic of the two stages of the adsorption process. At early times ($t < \tau_1$) the monolayer grows as a homogeneous hexagonal lattice. For $t > \tau_1$ rafts are formed, and the monolayer grows with contant interparticle distance.

as well as a decrease in the interparticle distance with time. This picture appears compatible with the data for early adsorption times, $t < \tau_1$. The second scenario is the growth of nanoparticle rafts at the interface. These rafts are organized in a compact hexagonal network, with a lattice constant that is independent of the number of nanoparticles in the cluster. A newly adsorbed nanoparticle joins the closest cluster, and occupies a hexagonal slot at the cluster edge. As a consequence, the interparticle distance does not evolve during the adsorption process, whereas surface tension decreases as the number of particles adsorbed at the interface increases. The experimental data suggest that the system is better represented by the raft-growth scenario for $t > \tau_1$. At the end of the adsorption process, surface tension and interparticle distance are approximately constant, suggesting a fully packed interface with a hexagonal network. The interparticle distance is then $d_\infty = 11.6$ nm, to be compared with the distance obtained if nanoparticle core-to-core contact is assumed ($2a_{\text{core}} \approx 4.5$ nm). This direct measurement of interparticle distance confirms previous results that suggest stretching of the grafted ligands at the interface.[15,18] Assuming that the nanoparticles are stabilized solely by steric repulsion between brushes, the interparticle distance at equilibrium writes $d_\infty = 2a_{\text{core}} + 2L$ (see Figure 1e) with $L \approx 3.5$ nm. This value is compatible with extended brushes as MUTEG ligands are composed of a total of 14 C-C, 9 C-O, one C-S, and one Au-S bonds, leading to a contour length of $L_{\text{brush}} \approx 3.9$ nm. As $L \sim L_{\text{brush}}$, the ligands grafted at the Au nanoparticle surface are assumed to be in the brush configuration. The thickness of the brush L can thus be converted into a grafting density $\sigma = L\rho N_A/M$ where $\rho = 997$ kg m^{-3} is the bulk density of the free ligand, N_A is the Avogadro constant, and $M = 380$ g mol^{-1} is the molar mass.[32] The grafting density is found to be $\sigma \approx 5.5$ chains nm^{-2}, in agreement with previous work.[18] A common way to quantify the stretching of the polymer brush is to compute the reduced tethered density $\Sigma = \sigma\pi R_g^2$ where $R_g \approx 0.36$ nm is the radius of gyration of the polymer in solution.[32] After adsorption, the reduced tethered density is found to be $\Sigma = 2.2$, corresponding to a brush with stretched ligands.

Rate-dependent dynamics upon surface compression. We investigated the impact of compression rate on the evolution of the interparticle distance and the surface pressure. The drops are created and incubated for 15 minutes (900 seconds) to allow for nanoparticle adsorption. The nanoparticle suspension is then flushed by flowing 10 mL of ultrapure water at 1 mL min^{-1}. The compression starts after acquiring the surface tension and the interparticle distance data for the initial state. The flow rate for withdrawal of the drop phase, which imparts the interfacial compression, was calibrated in order to achieve a constant rate of change of area during the experiment. Three different rates of compression were used: dA/dt = -0.0326, -0.0049 and -0.0016 mm^2 s^{-1}, referred to as fast, medium and slow, respectively. These rates correspond to initial values for the interfacial dilational strain rate $-\dot{\alpha} = (1/A_0)(dA/dt)$ = 4×10^{-3}, 6×10^{-4} and 2×10^{-4} s^{-1} respectively. The area evolution during compression for the three different experiments is shown in the inset of Figure 4a. The decrease is confirmed to be linear for the three different speeds. The experiments lasted 100, 530 and 1500 seconds for the fast, medium and slow compression respectively.

As shown in Figure 4a, for Π< 8 mN m^{-1} the surface pressure follows a similar evolution for all three compression rates and the curves overlap. The slope then decreases significantly, at different surface areas depending on the compression rates. The higher the compression rate, the earlier this change occurs. The apparent softening of the monolayer is due to a relaxation of the internal stress in the monolayer and may be explained either by expulsion of particles out of the interface, or by buckling of the monolayer. From the surface pressure curves, it is not possible to distinguish between the two phenomena. In summary, for $\Pi > \Pi_c$ desorption or buckling (out-of-plane events) are observed, with Π_c = 13 mN m^{-1}, Π_c= 12 mN m^{-1} and Π_c= 9 mN m^{-1} for the slow, medium and fast compression rates, respectively. In previous studies on the same system, desorption was observed for $\Pi > 13$ mN m^{-1}.[9]

The evolution of the interparticle distance during compression (Figure 4b) shows that, for the fast and medium compression rates, the distance decreases rapidly and plateaus to a value of 10.1 nm (L_{plateau}= 2.7 nm and σ_{plateau}= 4.2 chains nm^{-2}). On the plateau, further
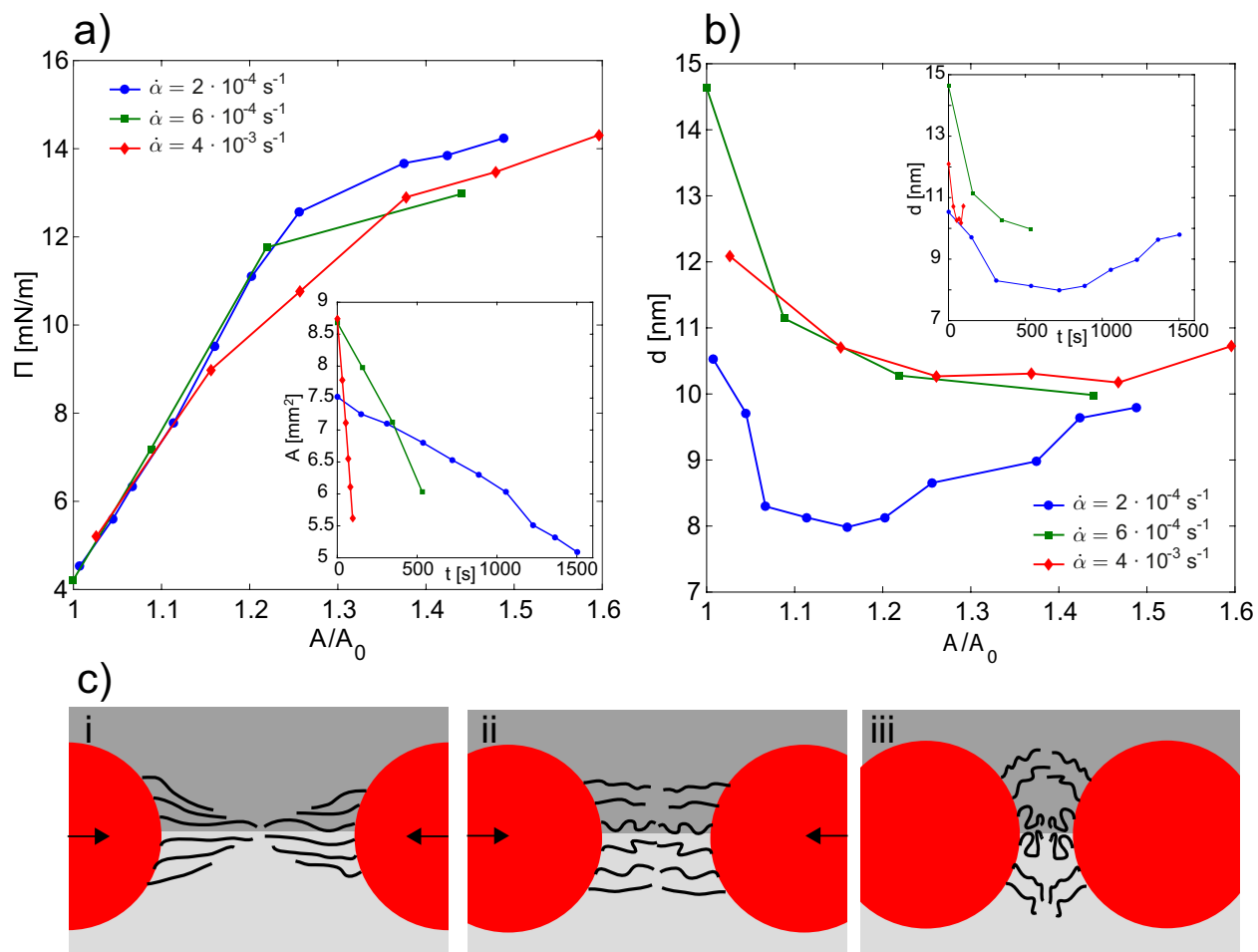
Figure 4: Surface compression at different rates. (a) Surface pressure Π as a function of the rescaled surface area A/A_0: ● slow ($\dot{\alpha} = 2 \cdot 10^{-4}$ s^{-1}); ■ medium ($\dot{\alpha} = 6 \cdot 10^{-4}$ s^{-1}); ◆ fast ($\dot{\alpha} = 4 \cdot 10^{-3}$ s^{-1}). Inset: measured drop area as a function of time. (b) Evolution of the interparticle distance d as a function of the rescaled surface area A/A_0. Inset: distance as a function of time. (c) Schematic of the transition of the grafted layer of ligands from a brush configuration (i) to a mushroom configuration (iii).

15

compression of the interface does not cause significant changes in the interparticle distance, again suggesting a major change at the interface. The fact that the distance between the nanoparticles at the interface does not decrease, is an indication that they are driven out of the plane of the interface. For the fast and medium compression rates, the reduced tethered density is $\Sigma_{\text{plateau}}= 1.7$, consistent with a brush configuration of the ligands.

In contrast, the slow compression experiment exhibits a very different behaviour. The interparticle distance decreases to a minimum value of $d_{\text{min}}= 8$ nm, well below the equilibrium value estimated during the adsorption process ($d_\infty= 11.6$ nm). This observation suggests the existence of a mechanism that allows either for a reduction in brush thickness, or brush interpenetration. To allow for a reduction of the brush thickness, the local density of the brush has to be reduced by ligands rearrangement. Two possible scenario may be envisioned, and may both be occurring during compression. Because the Au-S bond is mobile,[33] the ligands can reorganize over the surface of the particles. Ligand migration has been previously shown to occur on flat surfaces, although it is not clear what is the timescale for this process.[33] The other possible scenario for the ligand rearrangement is the bending of the chains that were previously stretched out at the interface towards the bulk phases. The experimental data do not allow us to exclude either scenario. The rearrangement of the ligands out of the interfacial region results in a decrease of density of the brush in the contact area (see Figure 4c (i)). Assuming that $d = 2a_{\text{core}} + 2L$ at any time in this slow process, the minimal brush thickness is found to be $L_{\text{min}}= 1.7$ nm. This converts into an effective local grafting density of $\sigma_{\text{min}}= 2.6$ chains nm^{-2} and thus $\Sigma_{\text{min}}= 1$. $\Sigma< 1$ is characteristic of a mushroom configuration (see schematics Figure 4c (ii)-(iii)), where the ligands are more free to form a coil, thus reducing the thickness of the brush. The interparticle distance reduction induced by the monolayer compression leads to ligand reorganization at high energetic cost, until out-of-plane rearrangements become more favorable. This can explain why d_{min} is bigger than the full mushroom state interparticle distance $d_{\text{coil}}= 5.3$ nm.

Brownian Dynamics simulations of compression at different Péclet numbers.
The different dynamics observed for different compression rates could be due to jamming of the nanoparticles in the monolayer. For sufficiently slow compression, the monolayer can always attain equilibrium (*i.e.* Brownian motion dominates at this time scale, favoring efficient packing), allowing for smaller interparticle distances to be reached. To investigate the role of rearrangements of the nanoparticles, we performed two-dimensional Brownian dynamics simulations of the monolayer, assuming that the nanoparticles are irreversibly adsorbed on the interface. We used the estimated surface coverage fraction based on the Au cores, $\Phi_0 \approx 0.15$, obtained from the measured interparticle distance of 11.6 nm, assuming hexagonal packing of the monolayer at the end of the adsorption process. Given the small compression rates $\dot{\alpha}(t = 0)$ used in the experiments, it is probable that the nanoparticle diffusion rate D/a_{core}^2 is faster than the characteristic compression rate. However, since the effective diffusion coefficient D of a ligand-grafted nanoparticle adsorbed at a fluid interface is not known, we performed simulations with different Péclet numbers $Pe = -\dot{\alpha}(0)\, a_{\text{core}}^2/D$ ranging from 10 to 10^{-2}, spanning both the fast and slow compression regimes. Figure 5 shows a comparison of the surface pressure Π obtained from the experiments at different compression rates, with that obtained from simulations for different Pe for one realization of the system with a number of nanoparticles N_d= 1500. We find a good agreement for the initial surface pressure and its initial slope, confirming that, close to equilibrium, the interparticle potential used and the parameters derived from the experiments describe the system satisfactorily. The surface pressure obtained from the numerical simulations constantly increases during the compression with an increasing slope, for all the Péclet numbers investigated. The increase in surface pressure follows from the stiffening of the interparticle repulsive force $-\frac{\partial U_{ij}}{\partial d_{ij}}\, \hat{\boldsymbol{d}}_{\boldsymbol{ij}}$ as the interparticle distance is reduced. The large surface pressure obtained at large Pe is explained by the fact that the nanoparticles do not have sufficient time to rearrange through diffusion, hence no relaxation of the stresses in the monolayer is possible. The results obtained for the surface pressure at $Pe = 0.01$ are in qualitative
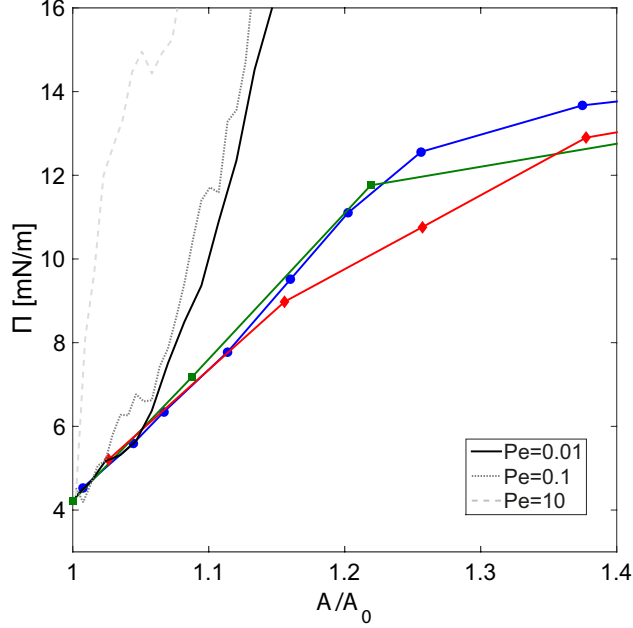
Figure 5: Surface pressure Π as a function of the rescaled surface area A/A_0. The symbols represent experimental data for different compression rates: $\bullet$ slow ($\dot{\alpha} = 2 \cdot 10^{-4}$ s^{-1}); $\blacksquare$ medium ($\dot{\alpha} = 6 \cdot 10^{-4}$ s^{-1}); $\blacklozenge$ fast ($\dot{\alpha} = 4 \cdot 10^{-3}$ s^{-1}). The lines represent results of two-dimensional Brownian Dynamics simulations for different Péclet numbers: $--$ Pe= 10, $\cdots$ Pe= 0.1 and $-$ Pe= 0.01.

agreement with the experiments at small A/A_0. However, at large A/A_0 the surface pressure measured in the experiments shows a softening rather than the stiffening obtained in the simulations. The simulations match reasonably well with the experiments for $\Pi <$ 7 mN m^{-1}, in agreement with the range of validity of similar simulations obtained in previous work. [18] We cannot unambiguously identify the mechanism responsible for the discrepancy observed in Figure 5 at higher pressures. A possible scenario is that Eq. (1) is a good approximation of the true interparticle potential energy only close to equilibrium, and it breaks down as the effects of ligand rearrangements become important. The breakdown of the assumption of irreversible nanoparticle adsorption could also be responsible for the deviation in Figure 5. This scenario implies that nanoparticles are expelled from the interface, or the monolayer buckles, thus relaxing the stresses in the monolayer to lower values compared to our numerical simulations. The simulation results clearly show that jamming cannot be responsible for the time-dependent behavior observed in the experiments as it implies a strong increase of

surface pressure already at early compression stages, which is not observed experimentally.

Out-of-plane reorganization of the particles. To further investigate the possibility of desorption of nanoparticles or monolayer buckling, the 2D pattern on the GISAXS detector is qualitatively discussed. As the surface becomes disordered, the correlation peaks broaden due to the higher dispersion of interparticle distances. Similarly, if the film becomes thicker either due to the formation of multilayers, or due to buckling, the lattice reflections tend to form a hexagonal pattern or a ring. Figure 6 shows three patterns obtained at different times during the compression for the three different rates. Pictures are extracted from the same data sets as the ones in Figure 4. For the fast compression (Figure 6a), the widening of the peak appears at $A/A_0 = 1.26$ where we start to observe the appearance of signal in the background. This signal intensity is further increased at $A/A_0 = 1.37$, filling a half-hexagon area delimited by the green dashed lines in Figure 6. This observation suggests the presence
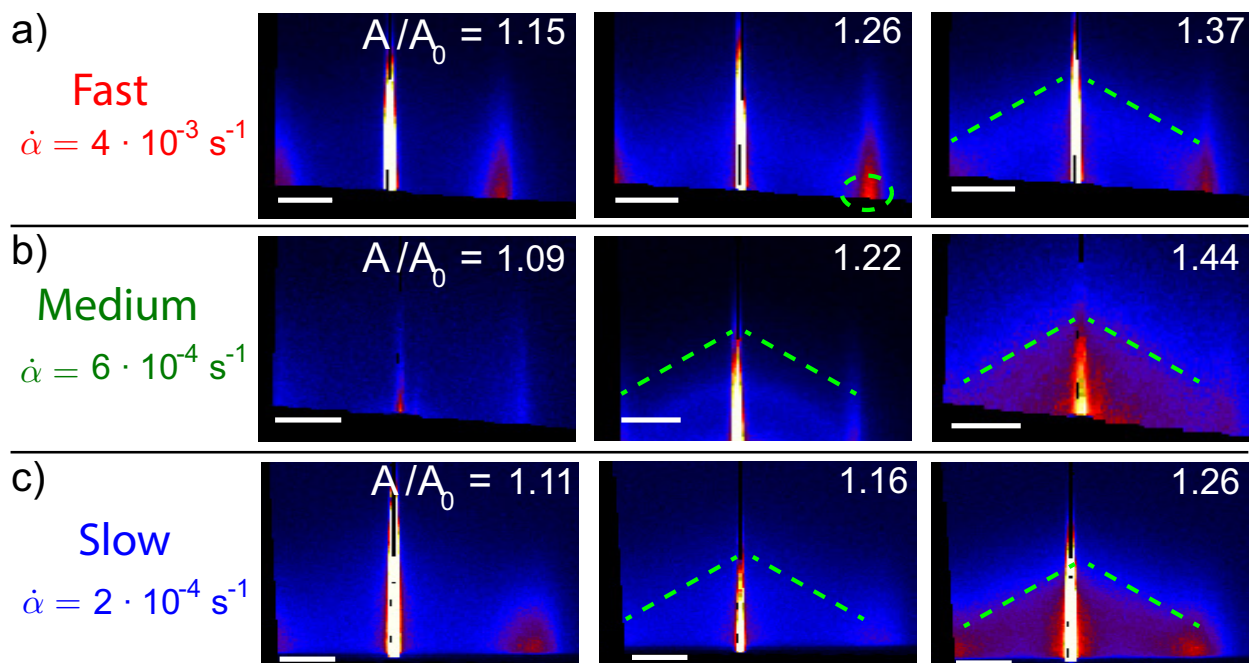

Figure 6: Evolution of the GISAXS pattern during monolayer compression at different rates. Features highlighted by green dashed lines are described in the text. (a) Fast compression, $\dot{\alpha} = 4 \cdot 10^{-3}$ s^{-1}. (b) Medium compression, $\dot{\alpha} = 6 \cdot 10^{-4}$ s^{-1}. (c) Slow compression, $\dot{\alpha} = 2 \cdot 10^{-4}$ s^{-1}. Scale bars: 0.04 nm^{-1}.

of nanoparticles in the vicinity of an ordered monolayer. Interestingly, these patterns are observed at the same A/A_0 as the deviation in the surface pressure isotherm (see Figure 4 and Figure 5). In the three experiments, we observed the signature of the out-of-plane events as soon as the interparticle distance reaches a minimum. Finally, it is shown that the intensity of this pattern is much stronger for the slower experiment at a given A/A_0. This observation points toward the creation of a thick film (multilayers) in this particular experiment. The three-dimensional structure that is formed alters significantly the correlation peak as can be seen in Figure 6c. This feature could explain why the interparticle distance is seen to increase again after $A/A_0 = 1.2$ in the slow compression experiment, as reorganization in multilayers allows for larger distance between the nanoparticles.

Summary and Conclusions

We have combined for the first time GISAXS and pendant drop tensiometry to characterize a nanoparticle monolayer on a dynamically deforming, curved fluid-fluid interface. The GISAXS scattering patterns give access to the interparticle distance at the interface. For each X-ray scattering pattern acquired, an optical image of the drop was simultaneously recorded, to obtain the corresponding surface tension from drop-shape analysis. With this method, we have studied the microstructure of a monolayer of ligand-grafted nanoparticles during adsorption from suspension, and upon area compression at different rates.

The adsorption experiment reveals that the interparticle distance becomes a constant after a time $\tau_1 = 2000$ s, while the surface tension continues to decrease over a longer time scale, $\tau_2 = 4200$ s. This behavior can be ascribed to the formation of particle rafts, where for increasing number of particles at the interface, the rafts grow while the interparticle distance remains a constant.

Compression of the monolayer at different rates results in non-equilibrium behaviors that could either be due to nanoparticle rearrangements within the monolayer, or to rearrange-

ments of the ligand brush on the nanoparticles. For small compression, the surface pressure as a function of surface area is found to be approximately independent of compression rate. However, in this early stage of compression a more prononunced, transient decrease in interparticle distance is observed for the slowest compression rate, which can be ascribed to ligand rearrangements. For sufficiently low compression rate, the ligands can either migrate because of the mobility of the thiol bond, or bend out of the plane of the interface, thus reducing the local ligand density in the contact region between the particles, and allowing the ligand brush to reorganize into a mushroom state. A reduction in the minimum interparticle distance is then possible. When the compression rate is high, the ligands remain in a brush configuration as they do not have time to rearrange or migrate, preventing the reduction of the distance through steric repulsion. Upon further compression, rate-dependent features in the surface pressure as a function of surface area are observed. We have run two-dimensional Brownian Dynamics simulations to assess the role of interparticle rearrangements on this behavior. The simulations deviate from the experimental results, as they predict much larger surface stresses upon compression than what is found in experiment. This discrepancy suggests that the assumption of a two-dimensional system breaks down, and the observed stress relaxation in the monolayer is due to out-of-plane displacements of the particles, either due to buckling of the monolayer or to particle expulsion. Qualitative analysis of the GISAXS patterns confirms the occurrence of out-of-plane events.

These insights into the dynamics of monolayers of ligand-grafted nanoparticles at fluid interfaces are of fundamental interest to understand the phase behavior of 2D soft matter systems, and should help optimize advanced materials and processes that exploit these nanoscale building blocks.

Acknowledgement

Supporting Information Available

- Figure S1: validation of X-ray contrast.

- Figure S2: GISAXS data pre-processing.

- Figure S3: error quantification for $q_{\parallel}$ data

- Figure S4: interaction potential for 2D Brownian Dynamics simulations

This material is available free of charge via the Internet at `http://pubs.acs.org/`.

References

(1) Herzig, E. M.; White, K. A.; Schofield, A. B.; Poon, W. C. K.; Clegg, P. S. Bicontinuous emulsions stabilized solely by colloidal particles. *Nature Materials* **2007**, *6*, 966–971.

(2) Haase, M. F.; Stebe, K. J.; Lee, D. Continuous Fabrication of Hierarchical and Asymmetric Bijel Microparticles, Fibers, and Membranes by Solvent Transfer-Induced Phase Separation (STRIPS). *Advanced Materials* **2015**, *27*, 7065–7071.

(3) Zhang, Y.; Wu, J.; Wang, H.; Meredith, J. C.; Behrens, S. H. Stabilization of liquid foams through the synergistic action of particles and an immiscible liquid. *Angewandte Chemie* **2014**, *126*, 13603–13607.

(4) Crossley, S.; Faria, J.; Shen, M.; Resasco, D. E. Solid Nanoparticles that Catalyze Biofuel Upgrade Reactions at the Water/Oil Interface. *Science* **2010**, *327*, 68–72.

(5) Turek, V. A.; Cecchini, M. P.; Paget, J.; Kucernak, A. R.; Kornyshev, A. A.; Edel, J. B. Plasmonic Ruler at the LiquidâĂŞLiquid Interface. *ACS Nano* **2012**, *6*, 7789–7799.

(6) Poulichet, V.; Huerre, A.; Garbin, V. Shape oscillations of particle-coated bubbles and directional particle expulsion. *Soft matter* **2017**, *13*, 125–133.

(7) Du, K.; Glogowski, E.; Emrick, T.; Russell, T. P.; Dinsmore, A. D. Adsorption Energy of Nano- and Microparticles at Liquid-Liquid Interfaces. *Langmuir* **2010**, *26*, 12518–12522.

(8) Luo, M.; Olivier, G. K.; Frechette, J. Electrostatic interactions to modulate the reflective assembly of nanoparticles at the oil-water interface. *Soft Matter* **2012**, *8*, 11923–11932.

(9) Garbin, V.; Crocker, J. C.; Stebe, K. J. Forced Desorption of Nanoparticles from an Oil–Water Interface. *Langmuir* **2012**, *28*, 1663–1667.

(10) Tao, A.; Sinsermsuksakul, P.; Yang, P. Tunable plasmonic lattices of silver nanocrystals. *Nature Nanotechnology* **2007**, *2*, 435–440.

(11) Kubowicz, S.; Hartmann, M. A.; Daillant, J.; Sanyal, M. K.; Agrawal, V. V.; Blot, C.; Konovalov, O.; Mohwald, H. Gold Nanoparticles at the Liquid- Liquid Interface: X-ray Study and Monte Carlo Simulation. *Langmuir* **2008**, *25*, 952–958.

(12) Razavi, S.; Cao, K. D.; Lin, B.; Lee, K. Y. C.; Tu, R. S.; Kretzschmar, I. Collapse of Particle-Laden Interfaces under Compression: Buckling vs Particle Expulsion. *Langmuir* **2015**, *31*, 7764–7775.

(13) Li, T.; Brandani, G.; Marenduzzo, D.; Clegg, P. Colloidal Spherocylinders at an Interface: Flipper Dynamics and Bilayer Formation. *Physical Review Letters* **2017**, *119*, 018001.

(14) Garbin, V.; Crocker, J. C.; Stebe, K. J. Nanoparticles at fluid interfaces: Exploiting capping ligands to control adsorption, stability and dynamics. *Journal of Colloid and Interface Science* **2012**, *387*, 1 – 11.

(15) Udayana Ranatunga, R. J. K.; Kalescky, R. J. B.; Chiu, C.-c.; Nielsen, S. O. Molecular Dynamics Simulations of Surfactant Functionalized Nanoparticles in the Vicinity of an Oil/Water Interface. *The Journal of Physical Chemistry C* **2010**, *114*, 12151–12157.

(16) Lane, J. M. D.; Grest, G. S. Spontaneous Asymmetry of Coated Spherical Nanoparticles in Solution and at Liquid-Vapor Interfaces. *Phys. Rev. Lett.* **2010**, *104*, 235501.

(17) Schwenke, K.; Isa, L.; Cheung, D. L.; Del Gado, E. Conformations and effective interactions of polymer-coated nanoparticles at liquid interfaces. *Langmuir* **2014**, *30*, 12578–12586.

(18) Garbin, V.; Jenkins, I.; Sinno, T.; Crocker, J. C.; Stebe, K. J. Interactions and Stress Relaxation in Monolayers of Soft Nanoparticles at Fluid-Fluid Interfaces. *Phys. Rev. Lett.* **2015**, *114*, 108301.

(19) Fuller, G. G.; Vermant, J. Complex Fluid-Fluid Interfaces: Rheology and Structure. *Annual Review of Chemical and Biomolecular Engineering* **2012**, *3*, 519–543, PMID: 22541047.

(20) Isa, L.; Calzolari, D. C. E.; Pontoni, D.; Gillich, T.; Nelson, A.; Zirbs, R.; Sanchez-Ferrer, A.; Mezzenga, R.; Reimhult, E. Core-shell nanoparticle monolayers at planar liquid-liquid interfaces: effects of polymer architecture on the interface microstructure. *Soft Matter* **2013**, *9*, 3789–3797.

(21) Narayanan, S.; Wang, J.; Lin, X.-M. Dynamical Self-Assembly of Nanocrystal Super-lattices during Colloidal Droplet Evaporation by in situ Small Angle X-Ray Scattering. *Physical Review Letters* **2004**, *93*.

(22) Jiang, Z.; Lin, X.-M.; Sprung, M.; Narayanan, S.; Wang, J. Capturing the crystalline phase of two-dimensional nanocrystal superlattices in action. *Nano letters* **2010**, *10*, 799–803.

(23) Jiang, Z.; He, J.; Deshmukh, S. A.; Kanjanaboos, P.; Kamath, G.; Wang, Y.; Sankara-narayanan, S. K.; Wang, J.; Jaeger, H. M.; Lin, X.-M. Subnanometre ligand-shell asymmetry leads to Janus-like nanoparticle membranes. *Nature materials* **2015**, *14*, 912.

(24) Costa, L.; Li-Destri, G.; Thomson, N. H.; Konovalov, O.; Pontoni, D. Real Space Imaging of Nanoparticle Assembly at Liquid–Liquid Interfaces with Nanoscale Resolution. *Nano letters* **2016**, *16*, 5463–5468.

(25) Daerr, A.; Mogne, A. Pendent Drop: An ImageJ Plugin to Measure the Surface Tension from an Image of a Pendent Drop. *Journal of Open Research Software* **2016**, *4*, e3.

(26) Allen, M. P.; Tildesley, D. J. *Computer simulation of liquids*; Oxford university press, 1989.

(27) Schultz, D. G.; Lin, X.-M.; Li, D.; Gebhardt, J.; Meron, M.; Viccaro, J.; Lin, B. Structure, wrinkling, and reversibility of Langmuir monolayers of gold nanoparticles. *The Journal of Physical Chemistry B* **2006**, *110*, 24522–24529.

(28) Vegso, K.; Siffalovic, P.; Majkova, E.; Jergel, M.; Benkovicova, M.; Kocsis, T.; Weis, M.; Luby, S.; Nygård, K.; Konovalov, O. Nonequilibrium phases of nanoparticle Langmuir films. *Langmuir* **2012**, *28*, 10409–10414.

(29) Luu, X.-C.; Yu, J.; Striolo, A. Nanoparticles adsorbed at the water/oil interface: coverage and composition effects on structure and diffusion. *Langmuir* **2013**, *29*, 7221–7228.

(30) Mukhopadhyay, M.; Hazra, S. Growth of thiol-coated Au-nanoparticle Langmuir monolayers through a 2D-network of disk-like islands. *RSC Advances* **2016**, *6*, 12326–12336.

(31) Rauh, A.; Rey, M.; Barbera, L.; Zanini, M.; Karg, M.; Isa, L. Compression of hard core–soft shell nanoparticles at liquid–liquid interfaces: influence of the shell thickness. *Soft Matter* **2017**, *13*, 158–169.

(32) Brittain, W. J.; Minko, S. A structural definition of polymer brushes. *Journal of Polymer Science Part A: Polymer Chemistry* **2007**, *45*, 3505–3512.

(33) Vericat, C.; Vela, M.; Salvarezza, R. Self-assembled monolayers of alkanethiols on Au (111): surface structures, defects and dynamics. *Physical Chemistry Chemical Physics* **2005**, *7*, 3258–3268.